Correspondence

CubeSat-Based Passive Bistatic Radar for Space Situational Awareness: A Feasibility Study

This paper proposes a low budget solution to detect and possibly track space debris and satellites in Low Earth Orbit. The concept consists of a space-borne radar installed on a cubeSat flying at low altitude and detecting the occultations of radio signals coming from existing satellites flying at higher altitudes. The paper investigates the feasibility and performance of such a passive bistatic radar system. Key performance metrics considered in this paper are: the minimum size of detectable objects, considering visibility and frequency constraints on existing radio sources, the receiver size, and the compatibility with current cubeSat's technology. Different illuminator types and receiver altitudes are considered under the assumption that all illuminators and receivers are on circular orbits.

I. INTRODUCTION

In the past 60 years, since the launch of Sputnik 1, the number of objects in orbit around the Earth has increased tremendously. A good part of these objects are classified as space debris representing a significant hazard for all current and future satellite missions [1]. In addition, the growing traffic is increasing the probability of collisions also among functioning satellites as the Iridium–Cosmos collision in 2009 demonstrated.

Even collisions with very small objects (a few centimetres in size) at orbital speed can cause catastrophic consequences. Each explosion or collision with space junk produces additional debris, which can lead to a cascade of more collisions. This chain reaction is known as *Kessler syndrome*, and some argue it has already started. Very large objects, such as defunct satellites, rocket bodies, and large fragments, can represent a threat even for people on the ground since they may hit the ground at unpredictable locations after reentry. In addition to trackable space debris, millions of nontrackable small fragments, with the size of

Manuscript received April 12, 2017; revised December 15, 2017 and April 30, 2018; released for publication May 10, 2018. Date of publication June 18, 2018; date of current version February 7, 2019.

DOI. No. 10.1109/TAES.2018.2848340

Refereeing of this contribution was handled by P. Singla.

This work was supported in part by the Engineering and Physical Sciences Research Council under Grant EP/K014307/1, and in part by the CUSPT project supported by the UK Space Agency under the NSTP2 call for exploratory ideas 2016.

Authors' addresses: A. R. Persico, P. Kirkland, C. Clemente, and J. J. Soraghan are with the University of Strathclyde, Centre for Signal and Image Processing, Electronic and Electrical Engineering, Glasgow G1 1XW, U.K., E-mail: (adriano.rosario.persico@gmail.com; paul.kirkland@strath.ac.uk; carmine.clemente@strath.ac.uk; j.soraghan@strath.ac.uk); M. Vasile is with the University of Strathclyde, Department of Mechanical & Aerospace Engineering, Glasgow G1 1XJ, U.K., E-mail: (massimiliano.vasile@strath.ac.uk). *(Corresponding author: Adriano Rosario Persico.)*

a grain of salt, exist that can penetrate the spacesuit of an astronauts or a window on a space vehicle with tragic consequences.

Information about space debris comes from a combination of ground-based and space-based measurements. One of the entities that identifies, tracks, and categorizes space objects is the United States Space Command [2], which consists of Space-Based Space Surveillance satellites and a network of radars and optical telescopes [3]. In 2009, the European Space Agency started a program for a European Space Situational Awareness System, which required the design of a radar system able to detect small targets with size in the order of one decimetre in LEO [3]. Moreover, in Europe, a number of radar systems are used to monitor space debris. An example is the bistatic radar (BR) system Grand Rseau Adapt la Veille Spatiale that has been operating in France since 2005. In Russia, 20 radars and telescopes are positioned in 8 different sites. In Germany, the Tracking and Imaging Radar system of Fraunhofer FHR allows for the estimation of target's characteristics as orbital elements, intrinsic motion parameters, target shape and size, and ballistic coefficient thanks to new signal processing techniques based on radar observations [3].

Among all sensors deployed to detect an track space debris radar systems represent an important contribution for their ability to provide high detection probabilities at very large ranges in addition to a range of target's characteristics.

The feasibility of tracking space debris by using a passive bistatic radar (PBR) was investigated in [4]. Specifically, [4] proposes a system, which comprises a ground-based receiver for space object tracking with low-power scattering observations of any objects above the horizon. The underlying principle is to estimate the radarcross section (RCS) of an object by measuring the received forward scattering (FS). The paper proposes several solutions to achieve a suitable signal-to-noise ratio (SNR) at the receiver, such as the use of multiple receiving elements and the integration of the received signal over time. One of the principal problem is represented by the Doppler offset of the received signal due to relative motion between transmitter, receiver, and target. Jayasimha and Jyothendar in [5] show the capability to detect small space debris by using a large-antenna earth-station communicating with a geo-stationary satellite, exploiting self-interference cancellation. Specifically, when a space debris is at near-LOS, the output of self-interference cancellation may contain the return from one or two debris, which can be used for detection. However, the presented method is dependent on weather conditions, since the debris signature can be affected by inadequate cancellation of direct-path caused by the clutter from weather. In [6], a novel multistep processing strategy is proposed with the aim of reducing computational costs for extracting target signature to an affordable level for a PBR. The first step comprises correlation with a replica of the expected signal for relative short integration times. After integrate and dump (I&D), the full length coherent integration is obtained by summing the outcomes from the two operations with the necessary phase adjustments.

The FS radar configuration represents a suitable countermeasure also to stealth technology. With an FS radar, one can detect objects with very small RCS, built with absorbing material [7]. In fact, the FS RCS of a target depends only on the size and the shape of its silhouette. Recently, FS radars have been exploited in many different scenarios to perform radar tasks, e.g., detection, tracking, and imaging. In [8], an algorithm for the classification of vehicles with different size is proposed based on different frequency Doppler shifts characterizing the target signature. In [9], the capability to detect an aircraft by a FS radar using the Global Navigation Satellite System (GNSS) satellites as illuminator of opportunity was demonstrated experimentally. Moreover, target classification was performed by evaluating the shadow inverse synthetic aperture radar image from received signals. Abdullah *et al.* in [10] show experimentally the capability of extracting microDoppler information due to target secondary motions, e.g., rotation or vibration, which may be used for target classification using FS configuration [11]. In this paper, the concept of FS is exploited for space situational awareness. A novel radar system for the detection of very small space debris, which may allow the development of target tracking and classification capabilities, is proposed. Specifically, the feasibility of a new space-borne PBR system for space target detection is investigated.

In the proposed system, the PBR is installed on one or more cubeSats flying at low altitude and receiving the RF signals transmitted by noncooperative illuminators at higher altitudes. The main motivation for a space-borne PBR is that:

1) it reduces the distance between transmitter and receiver;
2) allows for a lower relative velocity between illuminator and receiver;
3) bypasses the atmosphere and the sources of error and attenuation that come with it.

The long distance has an impact on the required gain of the antenna, while the relative velocity has an impact on the integration time, and thus the ability to detect small objects. A cubeSat-based PBR offers a low-cost alternative solution since the shorter distances and smaller relative velocities allow one to achieve suitable SNR with a simpler hardware and lower costs. The proposed system can provide higher integration times by conveniently selecting the system illuminator. Moreover, a space-borne receiver in LEO avoids the detection of other flying objects, and the degradations of the signal due to atmospheric effects. Finally, by using two or more cubeSats, one can observe the same target for different parts of its orbit improving temporal and spatial resolution. The paper will consider technologies that are compatible with mass and dimensions of cubeSats and a wide range of illuminators. The key performance metric, for the proposed system, is the minimum size of detectable target.

The remainder of the paper is organized as follows. Section II describes the proposed radar system configuration. In Section III, the capabilities of proposed system

are evaluated in terms of minimum detectable target's size while Section IV concludes the paper.

II. CUBESAT-BASED SPACE-BORNE RADAR SYSTEM

In this section, a new system for space debris detection and monitoring is introduced. The idea is to fly a receiver at low-altitude, collect, and analyze the radio waves coming from any satellite flying at higher altitudes and broadcasting toward the Earth. Such a system can be defined and operated as a PBR. In fact, PBRs are radar systems composed of only the receiver, which exploits RF energy transmitted by other noncooperative systems (generally a communication system) to perform radar tasks such as target detection, parameter estimation, imaging, and classification. PBRs are an interesting solution in many applications with tight power and weight constrains because they do not need a dedicated transmitter, are low cost, have low-power requirements, lighter payloads, and no dedicated frequency allocation requirement. PBR systems are, therefore, suitable to be installed on low-cost power-limited platforms like cubeSats. One or more cubeSats in LEO would form a low-cost detection system with a sufficient lifetime to collect enough data on the existing debris population but not long enough to increase such a population.

A. Radar Range Equation in Bistatic Configuration

A radar system is considered to be bistatic if there is sufficient separation between the transmitter and receiver antennas such that the angles or ranges to the target are sufficiently different [12]. The angle defined by the positions of transmitter, target, and receiver is known as bistatic angle, β (see Fig. 3). Since the performance of a radar system generally depends on the SNR at receiver sides, the radar range equation allows us to evaluate the expected SNR from a target at a specific range. Specifically, in case of bistatic configuration, the SNR for the single radar pulse is [13]

$$\text{SNR} = \frac{P_t G_t G_r \sigma \lambda^2 L_s}{(4\pi)^3 R_t^2 R_r^2} \frac{1}{P_n} \tag{1}$$

where P_t is the transmitted power by the system's illuminator, G_t and G_r are the gains in transmission and in reception, respectively, λ is the wavelength, σ is the RCS of the target, L_s (≤ 1) is a loss factor, which includes transmitter loss, propagation loss, receiver beam-shape loss, and signal processing losses. The product $P_t G_t$ known as effective isotropic radiated power (EIRP) representing the output power of an equivalent isotropic radiator, which generates the same transmitted flux in all directions. The RCS represents the area of target that produces energy scattered in the direction of the receiver. P_n is the noise power given by

$$P_n = kT_0 B_r F \tag{2}$$

with k the Boltzman's constant, T_0 the noise reference temperature, F the receiver noise figure, and B_r is the receiver bandwidth. Clearly, the SNR decreases as the RCS decreases. Therefore, in scenarios with targets with RCS very small the use of the FS radar provides better SNR [8], [14], [15]. For this reason the FS radar has a significant potential for the detection of small objects.

In this paper, the FS configuration is proposed to guarantee better performance in terms of SNR in the case of a specific class of targets of interest.

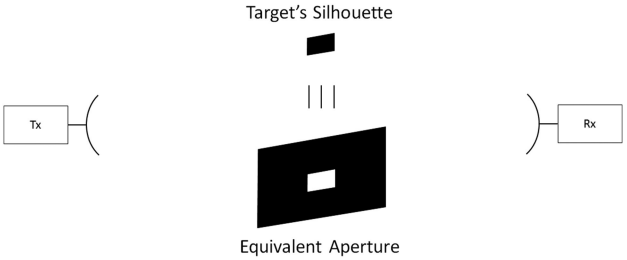

Fig. 1. Babinet's model for the forward-scatter case with $\beta = 180^\circ$.

B. Forward Scattering Configuration

FS occurs when β is in a neighborhood of 180°. This configuration guarantees a relative RCS enhancement since the FS depends only on the area and shape of the target's silhouette. The reason for this enhancement can be found in Babinet's principle, which affirms that, in optics, a perfect absorbing target diffracts the same electromagnetic wave as an aperture of the same shape and area A of the target (see Fig. 1) [13].

Two diffraction types are possible: Fraunhofer diffraction and Fresnel diffraction. In the former case, the target is electromagnetically far from both the transmitter and receiver, while in the latter case, the target is close to one of the two. Considering the following coefficients:

$$F_t = \frac{a^2}{R_t \lambda} \qquad F_r = \frac{a^2}{R_r \lambda} \tag{3}$$

where a is the greater dimension of the object, the Fraunhofer diffraction occurs when

$$F_t << 1 \qquad F_r << 1. \tag{4}$$

Under this conditions, the FS RCS can be written as [13]

$$\sigma_{\text{FS}} = \frac{4\pi A^2}{\lambda^2} = G_{\text{FS}} A \tag{5}$$

where G_{FS} represents the peak antenna gain of uniformly illuminated aperture whose area is equal to A. Then, within the Fraunhofer zone, the RCS, in the FS case, increases with the target section. When the bistatic angle is smaller than 180°, the forward-scatter RCS rollsoff from σ_{FS}. The rolloff is approximated by treating the shadow area A as a uniformly illuminated antenna aperture. More details can be found in [13].

C. Proposed Configuration

As illustrated in Fig. 2, the sensing platform comprises essentially three principal components: a software defined radio (SDR) as a PBR receiver, a low noise amplifier (LNA), and one or more antennas. The LNA is introduced to enhance the sensing capability by increasing the receiver gain.

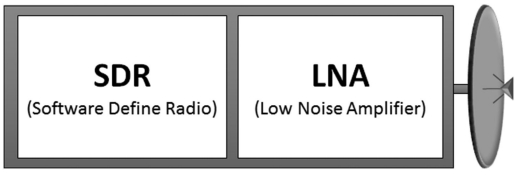

Fig. 2. Representation of proposed radar system for space debris detection and tracking.

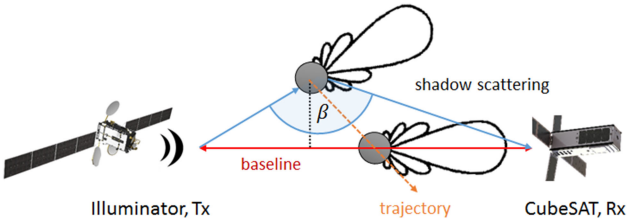

Fig. 3. Working principle of the proposed passive radar on cubeSat system.

Any satellite transmitting radio waves toward the Earth within the frequency band of the antenna on the sensing platform represents a suitable illuminator. The source of RF illumination can be selected statically or dynamically among the available platforms (e.g., existing constellations such as Iridium, GNSS, HY2A). One of the main features considered in this work for the illuminator selection, is the satellite altitude. In fact, the RF source has to fly at higher orbits with respect to the cubeSat, such that the FS region between transmitter and receiver can be exploited for the detection of space debris. By using the FS configuration, an object can be detected by measuring the variation in received power. When there is no object along the Line of sight (LOS) between transmitter and receiver, the received power is almost constant in time. When an object approaches the LOS, the FS field starts to shadow the receiver leading to a loss of received power. The proposed system configuration is described in Fig. 3. The peak FS RCS is reached when the target crosses the LOS and it is given by (5). This peak value can be used as a signature for the detectability of an object. Note, however, that even in the case in which the bistatic angle never reaches 180°, the detection via FS radar can take place considering the sidelobes effect of the diffracted field [8].

One of the critical drawbacks of FS radar is that this system does not allow one to estimate directly the target range. Nevertheless, the absence of range resolution is compensated by the advantage of absence of signal fluctuation because of the target's natural swinging, which represents a limit for coherent signal processing time in conventional radar. Furthermore, the FS radar allows power budget improvements as it allows for long integration intervals.

Notice that, in order to obtain the maximum benefit from a long coherent processing interval, the received signal must have a zero frequency offset with respect to the matched filter. By using a PBR on a cubeSat, the Doppler offset can be very small in case of transmitter, receiver, and target move along similar directions. Moreover, the attenuation and delays introduced into received signal by the atmosphere (e.g., by troposphere) are avoided.

In case the signal transmitted by the illuminator is known (e.g., GNSS), a way to achieve a good performance from a such passive system is to create a replica of the expected scattered signal from the debris for the receiving system, assuming a preliminary knowledge of system kinematic. However, since the Doppler effect that affects the received signal result from the relative movement of transmitter, receiver, and target (which can be about thousands of metres per second in the worst case of opposite fly directions), it is not guaranteed to yield a constant Doppler offset during the acquisition time interval. For this reason, a bank of matched filters could also be used, in case of small deviations from the expected Doppler, assuming linear variation [4].

An alternative approach is proposed in [6], where a multistep processing strategy is described for reducing the computational cost. First, the received signal is correlated with a replica of the expected signal over a relative short integration period. The latter is taken short enough such that the phase error between the received signal and the replica is approximately constant. Through I&D operations, complex observations of the beat signal between the replica and the actual indirect arrival are obtained. Finally, the full length coherent integration is obtained by adjusting the phase of the samples of I&D operations and summing over the observation period. This second step is robust against phase errors that are inconsistent over the observation period. This approach, which has been demonstrated in case of GNSS signals, can be potentially adapted for decoding other weak signals as well [6].

Another possible solution is the crystal video detector (CVD). The CVD consist into widely used detection scheme, based on the square law detector, followed by mean level cancellation and matched filter. Ustalli *et al.* in [16] present a full characterization of the performance of the CVD for a FS radar in presence of a moving target onto linear trajectory against Additive White Gaussian Noise. Specifically, it is shown that the CVD has limited losses with respect to the ideal detector, when the target is in far field. For this reason, this kind of detector can be used for the proposed system for monitoring a specific set of orbits at suitable distance from the cubeSat's orbits and the selected illuminator's ones.

III. DETECTION CAPABILITY ANALYSIS

In this section, the detection capabilities of the proposed radar system are evaluated. Before extracting the desired radar information, the SNR is generally increased by processing the received signal, e.g., matched filtering. Specifically, the signal processing gain, G_{sp} provided by the matched filter is approximately given by the product between the transmitted pulse length τ and the transmitter bandwidth B_t. In addition, several radar pulses can be integrated leading to higher value of the SNR at receiver. Then, considering the signal processing gain and the incoherent

integration of N pulses, the SNR is

$$\overline{\text{SNR}} = \frac{P_t G_t G_r \sigma \lambda^2 L_s}{(4\pi)^3 R_t^2 R_r^2 k T_0 B_r F} \sqrt{N} G_{sp}. \tag{6}$$

Note that, targets orbiting in space exhibit additional motion components on top of the basic Keplerian one. In particular, orbital perturbations, with a frequency higher than the orbital period, and attitude motion lead to a fluctuation of the area of the target's silhouette that is measured by the radar [17]. Therefore, an incoherent integration of radar pulses has to be considered in order to take into account the fluctuations of the target's silhouette.

A. Integration Time

The integration time is defined as the time interval needed to transmit and receive the integrated pulses to perform the radar detection. For a FS PBR, the maximum possible integration time is the interval during which the target is approximately along the LOS between the transmitter and the receiver.

The maximum integration time for the proposed system depends on the orbits of transmitter, receiver, and space target and on both transmitter and receiver antenna's pointing and patterns. In this subsection, we analze the maximum and minimum possible integration times assuming different orbit geometries. For simplicity, only circular orbits are considered. Furthermore, the bore sight of the transmitter is expected to be aligned with the nadir direction and the bore sight of the receiver antenna is aligned with the zenith direction.

Let us consider that at $t = 0$ transmitter, receiver, and target are aligned. The coordinate system $(\hat{X}, \hat{Y}, \hat{Z})$ is defined such that the plane $\hat{X}\hat{Y}$ contains the orbit flown by the receiver and the $\hat{X}$-axis is along the line going through the transmitter, receiver, and target at $t = 0$.

Considering the three orbit radii d_{rx}, d_{st}, and d_{tx}, which represent the distances from the Earth center to receiver, space target, and transmitter, then the position vectors of the three objects in the $(\hat{X}, \hat{Y}, \hat{Z})$ reference frame are defined as

$$\boldsymbol{p}_{rx}(t) = d_{rx} \begin{bmatrix} \cos(\omega_{rx} t) \\ \sin(\omega_{rx} t) \\ 0 \end{bmatrix}$$

$$\boldsymbol{p}_{st}(t) = d_{st} \begin{bmatrix} \cos(\omega_{st} t) \\ \sin(\omega_{st} t)\cos(\alpha_{st}) \\ \sin(\omega_{st} t)\sin(\alpha_{st}) \end{bmatrix}$$

$$\boldsymbol{p}_{tx}(t) = d_{tx} \begin{bmatrix} \cos(\omega_{tx} t) \\ \sin(\omega_{tx} t)\cos(\alpha_{tx}) \\ \sin(\omega_{tx} t)\sin(\alpha_{tx}) \end{bmatrix}$$

where ω_{rx}, ω_{st}, and ω_{tx} are the angular velocities of receiver, space target, and transmitter, respectively, and α_{st} and α_{tx} represent the squint angle with respect to the plane $\hat{X}\hat{Y}$ of the orbits of space target and transmitter. Note that the three orbits are coplanar if α_{st} and α_{tx} are 0 or π.

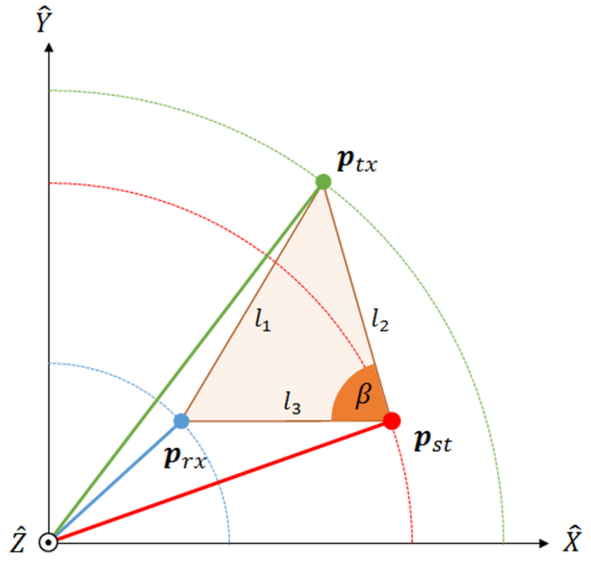

Fig. 4. Representation of the bistatic angle β between transmitter, receiver, and target moving on different orbits.

However, in the case of squint angle equal to π the orbits of transmitter and target are retrograde with respect to the one of the receiver.

The angular velocity ω_{orbit} for an object orbiting circularly around the Earth, hence the orbital period, depends only on the distance from the Earth centre d. In particular, according to Kepler's third law, it follows that

$$\omega = \omega(d) = \sqrt{\frac{\mu}{d^3}} \tag{7}$$

where μ is the gravity constant of the Earth. According to the Cosine Rule, the bistatic angle can be evaluated considering the relative distance between the three elements of the radar scenario (see Fig. 4), which are defined as follows:

$$l_1(t) = \|\boldsymbol{p}_{tx}(t) - \boldsymbol{p}_{rx}(t)\| \tag{8}$$

$$l_2(t) = \|\boldsymbol{p}_{tx}(t) - \boldsymbol{p}_{st}(t)\| \tag{9}$$

$$l_3(t) = \|\boldsymbol{p}_{st}(t) - \boldsymbol{p}_{rx}(t)\|. \tag{10}$$

Then, the bistatic angle is

$$\beta(t) = \cos^{-1}\left(\frac{l_2^2(t) - l_1^2(t) + l_3^2(t)}{2 l_2(t) l_3(t)}\right). \tag{11}$$

It is highlighted that since the Earth has not a perfect spherical shape, the transmitter and the receiver at different altitudes experience different precession of the line of the nodes [18]. Therefore, the orbits of transmitter, target, and receiver cannot remain coplanar, and the illuminator (the transmitter) needs to be selected dynamically to allow higher integration times.

B. Figure of Merit

The key performance indicator for the proposed PBR system is the minimum detectable target's size. From (6), the RCS can be written as a function of the system

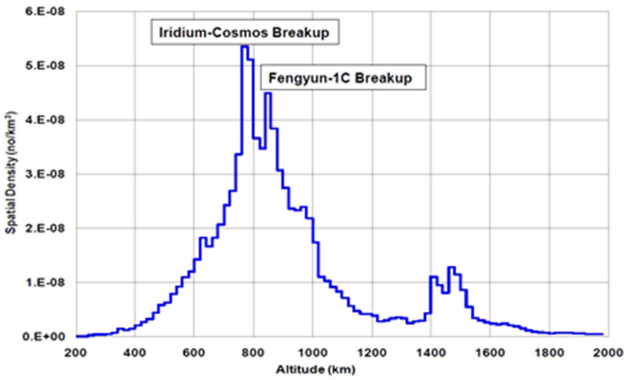

Fig. 5. Spatial density of objects in LEO, according to the 2011 NASA report to the United Nations Office for Outer Space Affairs [19].

parameters and SNR as follows:

$$\sigma = \frac{(4\pi)^3 R_t^2 R_r^2 k T_0 B_r F}{P_t G_t G_r \lambda^2 L_s} \frac{\overline{\mathrm{SNR}}}{\sqrt{N} G_{sp}}. \tag{12}$$

In this way, it is possible to define what the minimum RCS of a detectable target is by fixing the SNR at the receiver that is needed to guarantee a given probability of detection. Since in the case of FS, the RCS depends only on the target's silhouette area, the information on sizes of detectable object can be obtained from the RCS.

From (12), it is noted that the RCS is a function of the target's altitude. In particular,

$$\begin{aligned} \sigma_{\min} \propto R_t^2 R_r^2 &= f(\rho_{st} | \rho_{rx}, \rho_{tx}) \\ &= (\rho_{st} - \rho_{rx})^2 (\rho_{tx} - \rho_{st})^2 \end{aligned} \tag{13}$$

where ρ_{st}, ρ_{rx}, and ρ_{tx} are the altitudes of the target, the receiver, and the transmitter, respectively. Then, for a certain system, fixing the transmitter's and receiver's altitude the greatest value of minimum RCS is achieved when the object is in the middle of the baseline of the FS radar

$$\overline{\rho_{st}} = \frac{\rho_{rx} + \rho_{tx}}{2}. \tag{14}$$

Therefore, it is possible to detect objects with smaller RCS when they are closer to the receiver or to transmitter.

From (5), it follows that, for a FS system, the minimum target silhouette's area $\bar{A}$ in the Fraunhofer zone is obtained from the minimum required RCS as follows:

$$\begin{aligned} \bar{A} &= \sqrt{\frac{\lambda^2 \sigma_{\min}}{4\pi}} \\ &= \frac{4\pi R_t R_r}{\lambda} \sqrt{\frac{k T_o B_r F \ \widehat{\mathrm{SNR}}}{P_t G_t G_r G_{sp} L_s \sqrt{N}}} \end{aligned} \tag{15}$$

where $\widehat{\mathrm{SNR}}$ is the minimum SNR required to guarantee detection.

C. Observation Zone of Interest

From the current distribution of space objects in Fig. 5, one can see that the peak density in LEO is at an altitude of around 800 km. This spatial density was drastically increased by two impact events that generated as many as 6000 trackable objects [20]. The first was the deliberately destruction by a missile of the Chinese Feng-Yun weather satellite. The second impact was between the operational Iridium 33 mobile communications satellite and the defunct Russian Cosmos 2251 weather satellite.

Given the high density of objects in this orbit regime, without loss of generality, in this paper, we will consider targets flying in that region.

D. Selection of the Illuminators

The choice of the illuminators is driven by a number of parameters that concur to increase the SNR. For the design of the proposed system, the key selection criteria are the EIRP of the RF sources, their distance from the target and receiver, the carrier frequency (or wavelength), the system bandwidth, which determines the power of noise at the receiver, and the modulation scheme used by the source, which determines the signal processing gain and gain of the integration time.

In this paper, a set of two illuminators is considered for the analysis of performance. The first is the Haiyang-2A (HY2A), which is a second generation satellite series for ocean monitoring approved by the China National Space Administration, Beijing [21]. The satellite has been placed at an altitude of 971 km, on a near sun-synchronous frozen orbit, with an inclination of 99.3°. The orbital period is of 104.45 min. The HY2A is equipped with an active radio altimeter (RA), which works at two different frequencies (Ku-band and C-band). The altimeter uses the LF-chirps (low frequency) to perform its task with bandwidths of 320 MHz, 80 MHz, and 20 MHz in Ku-band and 160 MHz in C-band. The pulse duration is 102.4 μs, and the altimeter transmits with a pulse repetition frequency (PRF), which varies between 1 kHz and 4 kHz. Hence, the achievable signal processing gain with a pulse long 102.4 μ s is 45.15 dB for the 320 MHz wide pulse in Ku-band and 42.14 dB for the 160 MHz wide pulse in C-band.

The second set of illuminators is the global star (GS) constellation. GS is a LEO satellite constellation dedicated to satellite phone and low-speed data communications. Specifically, the system broadcasts with a C-to-S band transponder and receives with an L-to-C band transponder, respectively. The GS payloads have been placed at an altitude of about 1400 km, with an orbit inclination of about 52° and an Orbit Period-Nodal is about 114 min. Therefore, GS does not cover polar areas, due to the low-orbital inclination [22].

The GS Canada mobile-satellite network primary modulation and multiplexing method is Code-Division Multiple Access. The system operates in four distinct frequency bands [22], which are as follows.

1) The forward or down-link service from satellite to user terminal operates in a band of 16.5 MHz between 2483.5 MHz and 2500 MHz where there are 13 frequency-division multiplexed channels, each 1.23 MHz wide.

TABLE I
Link Budget Parameters

Parameter	Description		HY2A		GSTAR	
λ	Wavelength.	[mm]	22	57	43	120
G_r	Receiver antenna gain.	[dB]	34.03	25.78	28.15	19.30
$EIRP$	EIRP.	[dB]	52.5	47	19	37
B_R	Radar's Bandwidth.	[MHz]	320	160	180	16.5
G_{sp}	Signal processing gain.	[dB]	45.15	42.14	62.55	52.04
G_{LNA}	LNA gain.	[dB]	40	42	40	50
F	Radar's noise figure.	[dB]	10	10	10	12.5
k	Boltzmann's constant.	[J/K]	1.38×10^{-23}			
T_0	Noise reference temperature.	[K]	290			
L_s	Loss factor.		1			
SNR	SNR at radar receiver.	[dB]	10			

2) The return or up-link service from user terminal to satellite operates in the band between 1610 MHz and 1626.5 MHz.
3) The forward feeder link from feeder-link earth station to satellite occupies the band from 5091 MHz to 5250 MHz where there are eight channels 16.5 MHz wide in right-hand circular polarization and additional eight channels 16.5 MHz wide transmitted in LHCP.
4) The return feeder link from satellite to feeder-link earth station occupies the band 6875–7055 MHz with 16 frequency-division multiplexed RF channels, each one 16.5 MHz wide and associated with a separate antenna-pattern beam in the 1610–1626.5 MHz band.

For the system proposed, in this paper, the 16.5 MHz wide downlink, from satellite to user, in 2483.5–2500 MHz bandwidth and the 180 MHz wide return feeder link, from satellite to ground station, in 6875–7055 MHz are employed. Considering a signal segment of 10 ms for computing the radar detection, the two signal processing gain are 52.17 dB and 62.55 dB for the C-band and S-band downlink, respectively.

E. Numerical Results

For the numerical simulations, in this paper, we will consider a cubeSat equipped with a SDR with a noise figure of 8 dB [23] and LNAs, which guarantee a gain in the range of [40, 50] dB with a noise figure within [2, 4.5] dB in the bandwidth of the selected illuminators [24]–[26]. The receiving antenna could be either a high gain deployable parabolic dish, a foldable patch array or a membrane antenna [27]. Since deployable parabolic antennas exist for nanoSATs [28]–[30], in the following, a parabolic dish is considered as receiving antenna. In this case, the antenna gain is given by

$$G_r = \frac{4\pi \eta_p A_p}{\lambda^2} = \eta_e \left(\frac{\pi D}{\lambda}\right)^2 \tag{16}$$

where η_e is the antenna efficiency, A_p the physical aperture area, λ the wavelength, D the antenna diameter. By fixing the antenna diameter and efficiency, the gain of the receiving antenna is evaluated from (16) given the wavelength. For the following performance analysis, the efficiency η_e is set equal to 0.5 and the diameter D equal to 0.5 m. The total receiver gain is then given by the sum of the receiver antenna gain and LNA gain in dB domain. The values of all other parameters are reported in Table I. The loss factor is set equal to 1, which represents the best case in terms of system losses. The proposed system in fact overcomes the problem of atmosphere absorption, which represents one of the most relevant loss factors.

Fig. 6 show the minimum silhouette's area of detectable object as a function of the integration time, for Ku-band and C-band transmitted chirp signals from a HY2A satellite to cubeSats at different altitudes. Specifically, the receiver is placed at 300 km, 400 km, 500 km, and 600 km of altitude with the target at 800 km. It is worth noting that, since in the HY2A case, pulsed transmission is taken into consideration, the number of integrated pulses N is given by the product between the altimeter PRF and the duration of integration time. Fig. 6(a) shows that with one single chirp, the minimum value of the silhouette's area of detectable target is around 300 cm^2 for a receiver at 300 km and around 125 cm^2 for a receiver at 600 km. Integrating several pulses the performance improves significantly: it is possible to detect objects with a silhouette's area smaller than 50 cm^2 for integration times longer than 0.5 s. From Fig. 6(b), it can be seen that for this configuration the minimum possible silhouette's area is smaller than 150 cm^2 with an integration time longer than 1 s for all receiver's altitudes.

Fig. 7(a) and (b) show the minimum silhouette's area of detectable object as a function of the integration time for a C-band and S-band transmitted signal from a GS satellite to cubeSats at different altitudes.

In the GS case, which involves continuous transmission, sequential segments of 10 ms are incoherently integrated such that N is given by the ratio between the duration of the integration time and the length of the single segment. Fig. 7(a) shows that with a C-band signal, the minimum silhouette's area is around 3000 cm^2 if the integration time

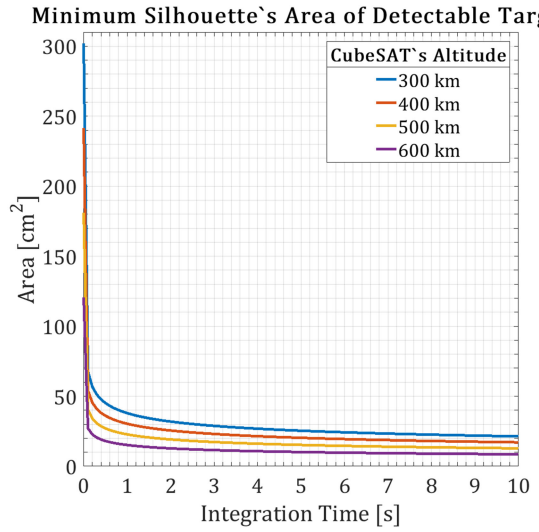

(a)

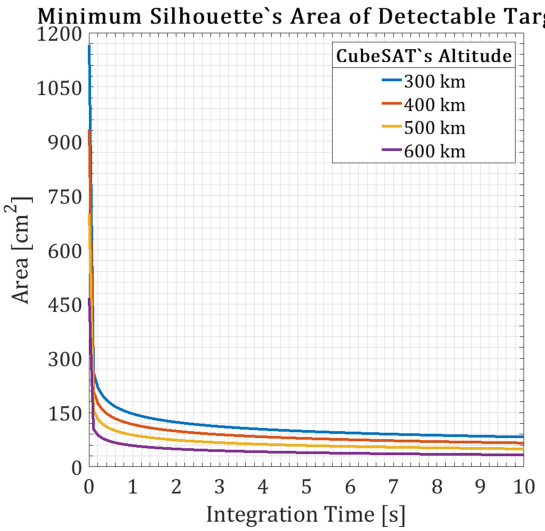

(b)

Fig. 6. Minimum silhouette's area of detectable target. (a) Ku-band. (b) C-band transmitted signal from a HY2A satellite to cubeSats at different altitudes.

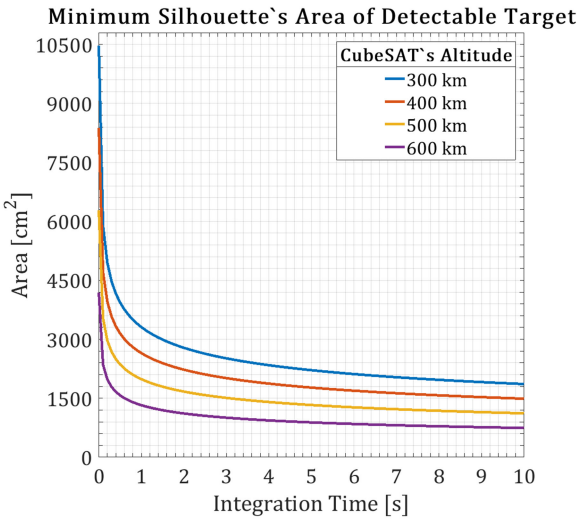

(a)

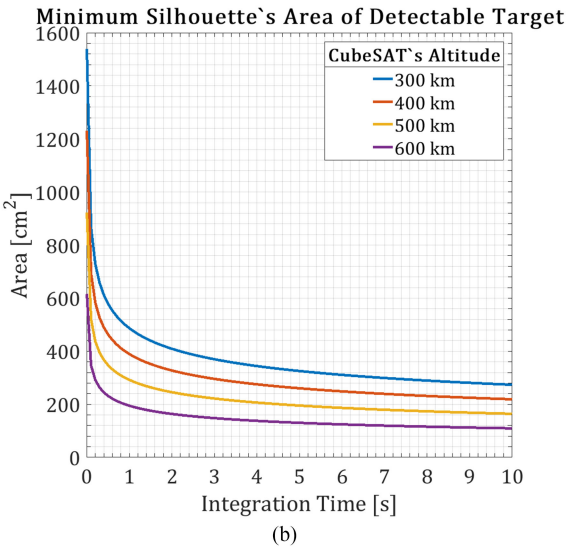

(b)

Fig. 7. Minimum silhouette's area of detectable target. (a) S-band. (b) C-band transmitted signals from a GS satellite as a function of cubeSat's altitude and integration time.

is over 5 s and the cubeSat is at 300 km, while it drops to 1000 cm^2 if the cubeSat is at 600 km. Fig. 7(b) shows that using the S-band signal by the GS, the silhouette's area of detectable target is smaller than 500 cm^2 for all the considered receiver's altitude and observation times greater than 2 s.

From Figs. 6(b) and 7(a), it is apparent the HYA2 illuminator allows for the detection of smaller targets, compared to the GS illuminator, since the latter is at higher altitude and transmits with a lower EIRP.

A measure of maximum integration time is obtained evaluating the duration of time interval during which the configuration of radar system is such that the bistatic angle is around 180°. Fig. 8 shows how the bistatic angle β varies on time considering the initial instant such that transmitter, receiver, and target are aligned. In particular, let us consider the general case of a transmitter at 1400 km (e.g., GS payload) from the Earth and the target at 800 km, as in the analysis described above, different values of the squint angles (α_{st}, α_{tx}) and receiver altitude are considered. It is easily noted that the possible integration time is longer when the orbits of three elements are coplanar and covered in the same direction. The worst case is obtained when the orbits are coplanar but the target moves in the opposite direction with respect to transmitter and receiver. The examples in Fig. 8 shows that increasing the cubeSat's altitude, the variation of bistatic angle becomes more sensitive with respect to squint angles of transmitter's and target's orbits. This trend is due to the greater cubeSat angular velocity obtained increasing the distance from Earth centre. Finally, it is worth noting that the gain in terms of sizes of detectable object, obtained by the incoherent integration, is more significant for shorter integration time. In particular, the detectable object's size is inversely proportional to the square root of the number of pulses incoherently integrated, N, being a function that decrease asymptotically to zero for

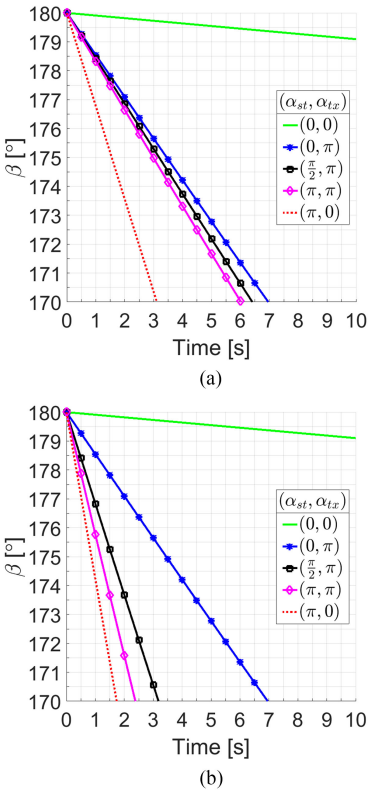

Fig. 8. Example of bistatic angle variation from the instant of alignment of transmitter, receiver, and target for different values of couple (α_{st}, α_{tx}); the transmitter is at 1400 km, target at 800 km, and receiver at 300 km (a), 600 km (b).

N tending to infinite. Then, for highest considered values of the N, the size of detectable object decreases slowly. Hence, it is possible to guarantee satisfactory system detection capability even for target moving in the opposite direction with respect to transmitter and receiver.

All the results can be reproduced using the methods and the information provided in the paper.

IV. CONCLUSION

In this paper, a feasibility study of a new space-based passive radar system for SSA was described. The proposed system comprises of a PBR deployed on a cubeSat, equipped with a SDR, and a passive antenna to perform radar task for space surveillance. The analysis of performance showed that the proposed system can represent a low-budget solution for the detection even of very small space objects with sizes of few centimetres. One of the most important aspect is that the relative shorter distances between transmitter, target, and space-based receiver with respect to a ground-based receiver guarantees higher SNR for the radar tasks. Moreover, the performance of the proposed system is not affected by atmospheric absorption due to the system geometry. For the same reason, the system functionality is independent of weather conditions and interference factor represented by flying man-made vehicles or bird flock.

The paper demonstrated that, with integration times shorter than 10 s and an appropriate choice of the illuminator, the system can detect objects with section areas as small as 50 cm^2 with a cubeSat positioned at 300 km and as small as 20 cm^2 if the cubeSat is at 600 km. Arguably, at the altitude of the space station or above the injection of cubeSats can potentially cause additional problems. Nonetheless, at the altitudes, considered in this paper, the expected lifetime of the receiver is such to limit the risk to increase the debris population. The capabilities of the system can be further improved by integrating signals from several illuminators. To this aim, wide-band antennas and suitable receiver filters have to be considered in order to recover all the received channels. Since the system capabilities depend on the distance between transmitter and receiver, the use of LEO emitters at higher orbits as illuminator of opportunity is most suitable for achieving better detection performance. The expected increase in LEO emitters, such as OneWeb, could represent an important factor for improving the performance of such a system. The proposed system may be used for a primary detection and identification of sensitive targets. FS radar has been used with success in literature for target discrimination based on Doppler analysis of echoes. Therefore, it is possible to classify targets by considering their microDoppler signature as a result of micromotions exhibited while orbiting.

Moreover, it is possible to use several cubeSat receivers working together in order to perform target localization and ranging. All this is the subject of a current investigation and will appear in future publications.

ADRIANO
ROSARIO PERSICO, *Student Member, IEEE*
PAUL KIRKLAND
CARMINE CLEMENTE, *Member, IEEE*
JOHN J. SORAGHAN, *Senior Member, IEEE*
University of Strathclyde, Glasgow, U.K.

MASSIMILIANO VASILE
University of Strathclyde, Glasgow, U.K.

REFERENCES

[1] European Space Agency, ESA, *Protecting Space Missions: The Challenge of Space Debris*. May 20, 2016. [Online]. Available: http://esamultimedia.esa.int/multimedia/publications/Space_Debris

[2] N. N. Smirnov and E. S. Institute
Space Debris: Hazard Evaluation and Mitigation. London, U.K.: Taylor & Francis, 2002.

[3] J. Ender, L. Leushacke, A. Brenner, and H. Wilden
Radar techniques for space situational awareness
In *Proc. 12th Int. Radar Symp.*, Sep. 2011, pp. 21–26.

[4] C. R. Benson
Enhancing space situational awareness using passive radar from space based emitters of opportunity
In *Proc. Mil. Commun. Inf. Syst. Conf.*, Nov. 2014, pp. 1–5.

[5] S. Jayasimha and P. Jyothendar
Detection of orbital debris using self-interference cancellation residual signal
In *Proc. IEEE Int. Conf. Sp. Sci. Commun.*, Jul. 2013, pp. 124–127.

[6] M. S. Mahmud, S. U. Qaisar, and C. Benson
Affordable processing for long coherent integration of weak debris-scattered GNSS signals with inconsistent doppler
In *Proc. Annu. IEEE Syst. Conf.*, Apr. 2016, pp. 1–6.

[7] R. S. Fadeev, A. V. Myakinkov, A. G. Ryndyk, and A. G. Ogurtsov
Detection and tracking of low-observable targets via multistatic forward scatter radar with airborne positions
In *Proc. 16th Int. Radar Symp.*, Jun. 2015, pp. 242–247.

[8] M. Cherniakov, R. S. A. R. Abdullah, P. Jancovic, M. Salous, and V. Chapursky
Automatic ground target classification using forward scattering radar
IEE Proc.—Radar, Sonar Navigat., vol. 153, no. 5, pp. 427–437, Oct. 2006.

[9] C. Hu, C. Liu, R. Wang, L. Chen, and L. Wang
Detection and SISAR imaging of aircrafts using GNSS forward scatter radar: Signal modeling and experimental validation
IEEE Trans. Aerosp. Electron. Syst., vol. 53, no. 4, pp. 2077–2093, Aug. 2017.

[10] R. S. A. R. Abdullah, A. Alnaeb, A. A. Salah, N. E. A. Rashid, A. Sali, and I. Pasya
Micro-Doppler estimation and analysis of slow moving objects in forward scattering radar system
Remote Sens., vol. 9, no. 7, 2017.

[11] C. Clemente and J. J. Soraghan
GNSS-based passive bistatic radar for micro-Doppler analysis of helicopter rotor blades
IEEE Trans. Aerosp. Electron. Syst., vol. 50, no. 1, pp. 491–500, Jan. 2014.

[12] *IEEE Standard Radar Definitions*, *IEEE Standard 686, 2008 (Revision of IEEE Standard 686, 1997)*, pp. c1–41, May 2008.

[13] N. Willis
Bistatic Radar(Series Electromagnetics and Radar). Institution of Engineering and Technology, 2005. [Online]. Available: https://books.google.co.uk/books?id=U0XG5WB-vY8C

[14] I. Suberviola, I. Mayordomo, and J. Mendizabal
Experimental results of air target detection with a GPS forward-scattering radar
IEEE Geosci. Remote Sens. Lett., vol. 9, no. 1, pp. 47–51, Jan. 2012.

[15] R. R. Abdullah and A. Ismail
Forward scattering radar: Current and future applications
Int. J. Eng. Technol., vol. 3, no. 1, pp. 61–67, 2006.

[16] N. Ustalli, P. Lombardo, and D. Pastina
Detection performance of forward scatter radar using a crystal video detector
IEEE Trans. Aerosp. Electron. Syst., vol. 54, no. 3, pp. 1093–1114, Jun. 2018.

[17] Q. Zhan, Y. Luo, Y. Chen
Butterworth-Heinemann, SciTech Publishing Inc., 2016.

[18] D. Vallado
Fundamentals of Astrodynamics and Applications, 3rd ed., vol. 21. New York, NY: Springer-Verlag, 2007.

[19] NASA. (2011) USA space debris environment, operations, and policy updates. [Online]. Available: http://www.unoosa.org/pdf/pres/stsc2011/tech-31.pdf

[20] J. Pelton
Space Debris and Other Threats from Outer Space (Series SpringerBriefs in Space Development). New York, NY: Springer-Verlag, 2013.

[21] ESA. (2000–2016) Eoportal directory. [Online]. Available: https://directory.eoportal.org/web/eoportal/satellite-missions/

[22] Description of globalstar system. Dec. 7, 2000. [Online]. Available: https://gsproductsupport.files.wordpress.com/2009/04/description-of-the-globalstar-system-gs-tr-94-0001-rev-e-2000-12-07.pdf

[23] E. Research^{TM}. Usrp e312. [Online]. Available: https://www.ettus.com/content/files/USRP_E312_Datasheet.pdf. Accessed on: Jun. 26, 2018.

[24] RF-LAMBDA. [Online]. Available: http://www.rflambda.com/. Accessed on: Jun. 26, 2018.

[25] RFCCOMP.com. Part of the HD communications group. [Online]. Available: http://www.rfcomp.com/hd29075.aspx. Accessed on: Jun. 26, 2018.

[26] RFCCOMP.com. Part of the HD communications group. [Online]. Available: http://www.rfcomp.com/hd30516.aspx. Accessed on: Jun. 26, 2018.

[27] Y. Rahmat-Samii, V. Manohar, and J. M. Kovitz
For satellites, think small, dream big: A review of recent antenna developments for cubesats.
IEEE Antennas Propag. Mag., vol. 59, no. 2, pp. 22–30, Apr. 2017.

[28] Composite technology development, Inc. [Online]. Available: http://www.ctd-materials.com/wordpress/?page_id=76.. Accessed on: Jun. 26, 2018.

[29] J. Sauder
Ultra-compact Ka-band parabolic deployable antenna (kapda) for cubeSats
In *Proc. iCubeSat Workshop, Pasadena, CA*, May 24–27, 2014. [Online]. Available: https://icubesat.files.wordpress.com/2014/06/icubesat-org_2014_b-1-4-kupda_sauder_20140617.pdf

[30] J. Harvey and M. D. Colleen Harvey
A deployable High gain reflectarray (DaHGR) antenna. [Online]. Available: https://marscubesatworkshop.jpl.nasa.gov/static/files/presentation/Harv ey-Thomas/deployable.pdf. Accessed on: Jun. 26, 2018.